JOURNAL OF AIRCRAFT
Vol. 29, No. 4, July–Aug. 1992

Design Load Predictions on a Fighter-Like Aircraft Wing

S. Agrawal,* P. J. Malloy,† and D. F. Fuglsang†
McDonnell Douglas Corporation, St. Louis, Missouri 63166

Numerical solutions for a transonic design condition have been obtained for a fighter-like aircraft wing geometry using Euler and Navier-Stokes equations. Both rigid and flexible wings are considered. Effects of viscosity and static aeroelasticity on the component loads such as shear, bending moment, and torsion, as well as hinge moments on the flaps and ailerons, are predicted. The flexible wing solutions are obtained by coupling the flow solvers with a simple NASTRAN model. Effects of fuselage and horizontal tail have also been obtained for the rigid wing case using Euler equations. The computed results are compared to available flight test data. It is found that the static aeroelasticity has only a minor role, whereas the effect of viscosity is very pronounced. Comparison with the flight test data is found to be best when viscous effects are included.

Introduction

THE prediction of aerodynamic loads for structural design is a challenging application of computational fluid dynamics (CFD) technology. In recent years, CFD has progressed to the point where structural loads can be computed on complex aircraft configurations using either the Euler or Navier-Stokes equations.[1,2] However, due to limitations in CFD algorithms and computing resources, the practical use of CFD capability for structural design loads has not yet been fully realized. The results presented here document recent progress in a continuing effort to define the optimal role of CFD for generating structural design loads as well as to determine the effects of aeroelasticity on design loads.

The approach was to apply state-of-the-art CFD methods to the fighter-like aircraft by starting with a wing alone geometry, and then to assess the impacts of grid density, interference, viscosity, and flexibility on the loads. This was done in a systematic fashion so that the differences in the loads between each calculation could be determined. All the computations were performed at a freestream Mach number of 0.90 and an angle-of-attack of 10 deg, which corresponded to a flight condition with a very high wing loading. For this condition, the inboard and outboard leading edge flaps were deflected down by 6.0 deg, whereas the trailing edge flap was deflected down by 7.5 deg. The aileron was not deflected. This point was chosen because it is typical of design points for fighter aircraft. The quality of loads from each calculation was assessed by a direct comparison with measured flight test loads.

Results from this study are presented in detail here. The next section presents Euler solutions for the rigid wing, wing-fuselage, and wing-fuselage-horizontal tail geometries. This provided the interference effects of the fuselage and the tail on the wing component loads. In order to assess the impact of viscosity, Navier-Stokes solutions for the rigid wing alone geometry were obtained.

The aircraft analyzed here is considered to have a relatively flexible structure. Due to this flexibility and the flight conditions chosen for the analysis, it was believed that aeroelastic effects may have a large impact on the accurate computation of component loads. For this reason, a static aeroelastic analysis was considered an integral part of the study. The procedure used, similar to the methods of Whitlow and Bennett[3] and Tatum and Giles,[4] involves coupling either the Euler or Navier-Stokes aerodynamic methods with a simplified finite element structural analysis. Detailed discussions of the computed loads with Euler and Navier-Stokes solutions, and comparison with the flight test data are presented in this paper.

Euler Solutions (Rigid Geometry)

Euler solutions on the rigid wing geometry are presented in this section. At the outset of the study, the interference effects due to the other components of the aircraft were also believed to be important. Therefore, to include effects of more complete geometry, a wing-fuselage and a wing-fuselage-horizontal tail configuration were also analyzed.

The flow solver chosen for this purpose was FLO67,[5] which has been found to be computationally very efficient for steady-state solutions. The code is based on a central-difference scheme. It integrates the discretized Euler equations using a cell-vertex finite volume scheme, maintaining conservations of mass, momentum and energy in each grid cell. Convergence to steady-state is accelerated with the use of an explicit five-stage Runge-Kutta scheme, residual smoothing, enthalpy damping, and multigrid. Like other central-difference schemes, FLO67 adds the dissipation terms explicity to the governing equations.

For each solution, a global C–H type grid was used. Prior to obtaining final solutions, a grid refinement study was conducted on the wing alone geometry in order to determine the proper grid dimensions and its distribution in the chordwise and spanwise directions of the wing. The grid density was varied in all three directions, one direction at a time, and the resulting component loads computed. From that study, it was concluded that FLO67 requires at least 80 chordwise and 25 spanwise points on each surface (upper and lower) for accurate prediction of loads. The grid dimensions used for the FLO67 calculations were 225 (streamwise), 33 (normal), and 33 (spanwise), resulting in a total of 169 chordwise (upper and lower) and 25 spanwise points on the wing surface. These points were clustered near the leading and trailing edges and near the wing tip. It should be noted that similar point distributions were also used on the wing-fuselage and wing-fuselage-tail geometries, resulting in grid dimensions of 429 (streamwise), 33 (normal), and 33 (spanwise). Figure 1 shows the surface grid on the wing alone geometry. The grid for the wing-fuselage geometry was the same as that for the wing-fuselage-tail, except that the tail was absent. Since no attempt was made to model the mass flow through the inlet, the ge-

Received Feb. 10, 1991; revision received Sept. 17, 1991; accepted for publication Sept. 20, 1991.

*Technical Specialist, Aerodynamics, CFD Project. Associate Fellow AIAA.

†Senior Engineer, Structural Dynamics, McDonnell Aircraft Company. Member AIAA.

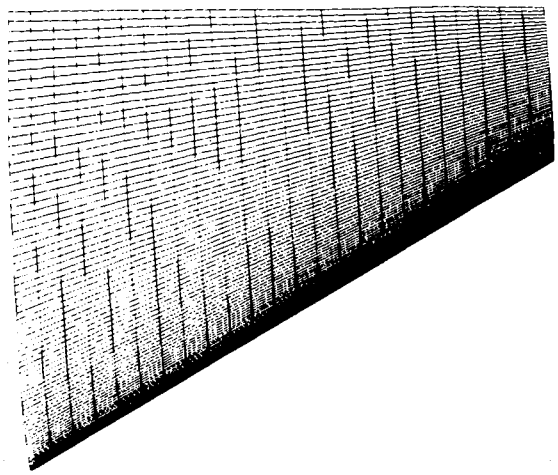

Fig. 1 Surface grid for the fighter-like wing geometry. Grid size: 225 × 33 × 33.

ometry in that region was faired over. For these configurations, the code I3G[6] was used to generate the six surfaces of a single zone C–H grid, and the EAGLE code[7] was employed to generate the interior points of this grid. The flow solutions were obtained with a modified version of FLO67.

Computed results from FLO67 for these geometries are shown in Figs. 2 and 3. Pressure contours on the wing upper surface due to the wing alone, wing-fuselage, and wing-fuselage-tail solutions are shown in Figs. 2a–2c. The chordwise pressure distributions at two semispan locations are plotted in Fig. 3. It is clear that the effect of fuselage on the wing flowfield is quite significant, and addition of tail to the wing-fuselage geometry does not affect the solution appreciably. The wing-fuselage and wing-fuselage-tail solutions are very similar; however, the overall loads are altered. On the inboard portion of the wing, the shock strengths are weakened and the location of the trailing edge shock is predicted slightly upstream due to the added geometry. On the other hand, on the outboard portion of the wing, the solution is practically unaltered. For all of these calculations, the average residuals were reduced by at least four orders of magnitude. The CPU hours required on a Convex C-1 computer were approximately 4.0, 7.0, and 10.0, for the wing alone, wing-fuselage, and wing-fuselage-tail solutions, respectively. The surface pressures computed from these solutions were integrated to obtain aerodynamic loads.

Navier-Stokes Solutions (Rigid Geometry)

At the outset of this study, the objective was to obtain Euler solutions on an almost complete geometry of the fighter-like aircraft. However, the loads computed from the Euler solutions did not compare well against the flight test data (discussed in the Comparison Against Experiment section). Therefore, effort was directed toward assessing the effect of viscosity, using a Navier-Stokes solver. The flow solver used for this purpose was TLNS3D,[8] again chosen for its computational efficiency. The methodology used in TLNS3D is very similar to that in FLO67, except that it integrates the thin-layer Navier-Stokes equations, and is based on a cell-center scheme.

The grid topology used for TLNS3D solutions was a C–O type, generated using the WGRID code based on the method of Eriksson.[9] This topology has been used to accurately model the wing tip flowfield. The dimensions of the grid were 193 (streamwise), 49 (normal), and 33 (spanwise), resulting in a total of 145 × 33 points on the wing surface. TLNS3D solutions were obtained with a Johnson-King turbulence model, which is an algebraic non-equilibrium model.[10] This model has been successfully applied in computing separated flowfields on wings.[11] Approximately 2.0 CPU hours on a Cray-2 computer of the Numerical Aerodynamic Simulation (NAS) facility were required.

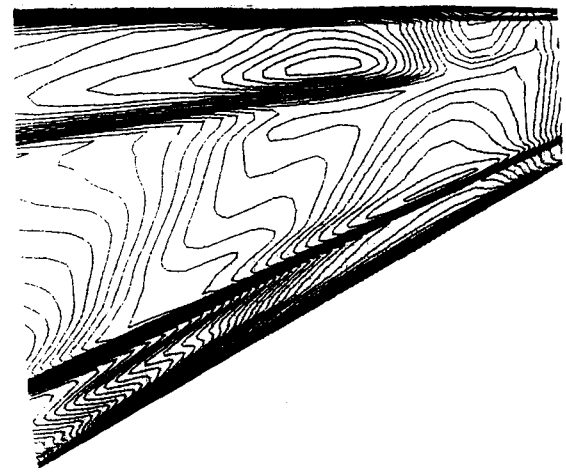

Fig. 2a Pressure contours on the (rigid) wing upper surface, FLO67 wing alone solution. $M_\infty = 0.90$, $\alpha = 10$ deg.

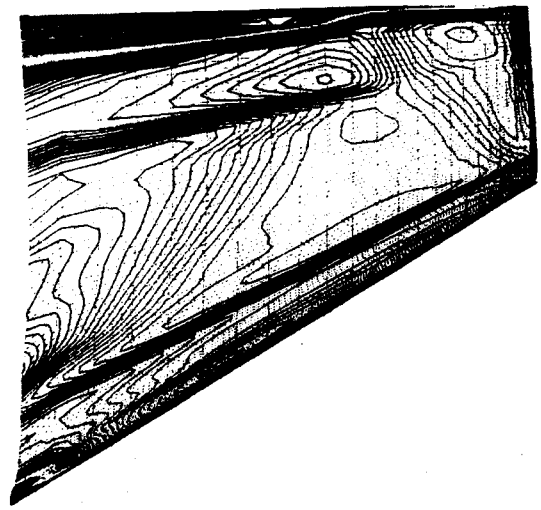

Fig. 2b Pressure contours on the (rigid) wing upper surface, FLO67 wing-fuselage solution. $M_\infty = 0.90$, $\alpha = 10$ deg.

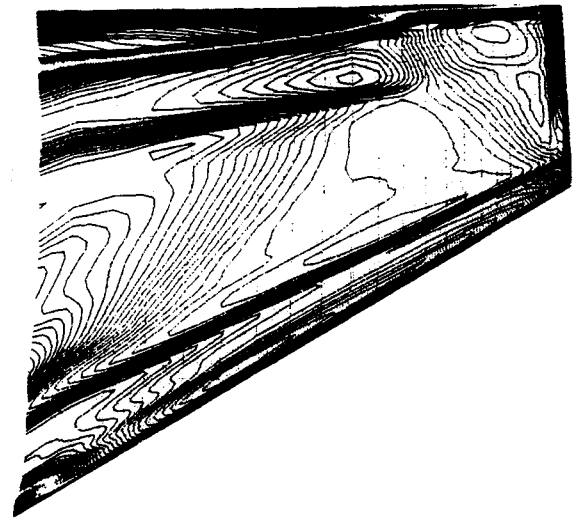

Fig. 2c Pressure contours on the (rigid) wing upper surface, FLO67 wing-fuselage-tail solution. $M_\infty = 0.90$, $\alpha = 10$ deg.

Figures 4 through 6 show the solutions obtained from TLNS3D. The pressure contours on the wing upper surface are shown in Fig. 4. Significant differences between the Euler and Navier-Stokes solutions are observed (Figs. 2 and 4). The shock-induced separated flow region is clearly visible in Fig. 5, which shows the computed streamline pattern. Due to massive separation on the upper surface, the shock strength and

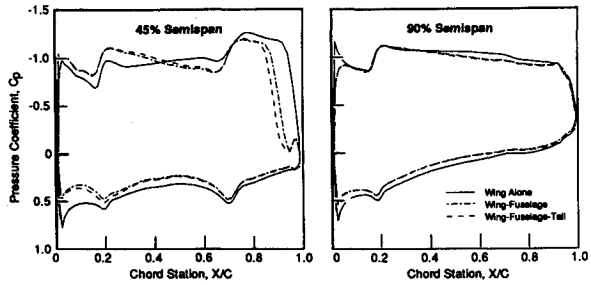

Fig. 3 Pressure distributions at two spanwise stations for wing alone, wing-fuselage, and wing-fuselage-tail geometries. $M_\infty = 0.90$, $\alpha = 10$ deg.

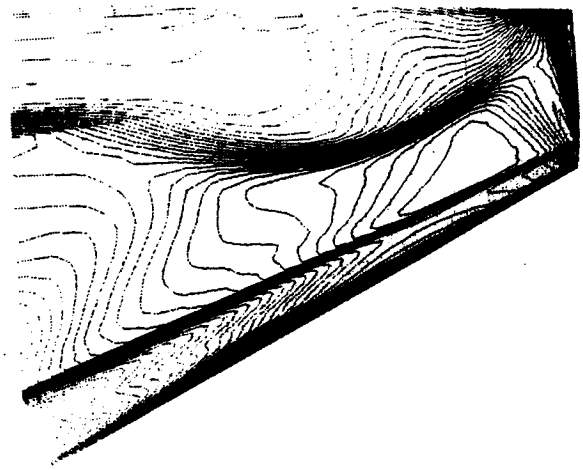

Fig. 4 Pressure contours on the (rigid) wing upper surface, TLNS3D solution. $M_\infty = 0.90$, $\alpha = 10$ deg, $Re = 80$ million.

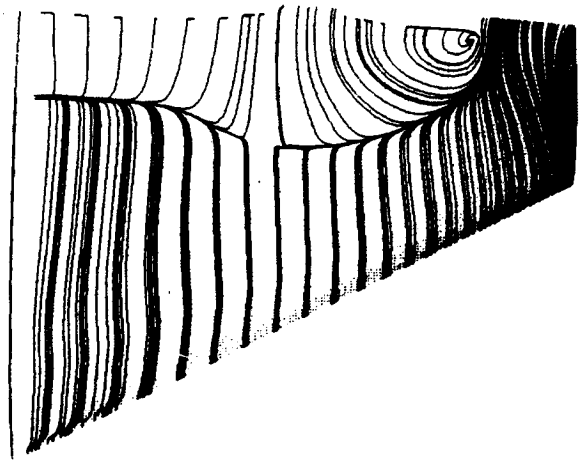

Fig. 5 Particle traces on the (rigid) wing upper surface, TLNS3D solution. $M_\infty = 0.90$, $\alpha = 10$ deg, $Re = 80$ million.

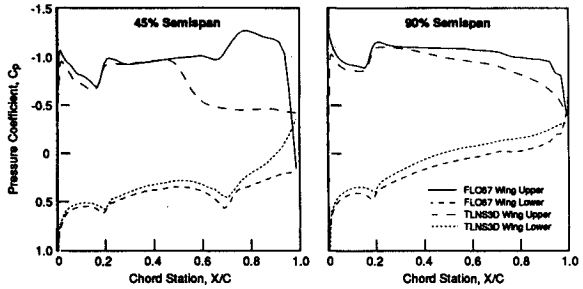

Fig. 6 Wing pressure distributions on the rigid geometry at two spanwise stations, FLO67 and TLNS3D solutions. $M_\infty = 0.90$, $\alpha = 10$ deg.

location are predicted very differently between Euler and Navier-Stokes solutions. Viscous effects also reduce the shock strength considerably with shock location upstream of that predicted using FLO67 (Fig. 6).

Euler and Navier-Stokes Solutions (Flexible Geometry)

To assess the effect of flexibility on the structural design loads, a simplified static aeroelastic analysis was performed on the wing alone geometry. The analysis involved coupling of a nonlinear aerodynamic theory with a linear structural analysis program. The aerodynamic solutions were computed using the FLO67 and the TLNS3D codes with computational grid sizes of 161 × 25 × 25 and 193 × 33 × 49, respectively. The deflections of the wing were calculated using a simple finite element representation of the structure. An iterative solution procedure was employed to obtain consistent aerodynamic loads and structural deflections at the specified flight condition.

In this study, the structure of the aircraft wing was idealized using the NASTRAN[12] finite element program. While the basic model was a simple beam-rod idealization, it also included the leading-edge flaps, trailing-edge flap, and aileron. The wing root was rigidly constrained to minimize inertia effects.

The iterative solution procedure for the aeroelastic analysis required the passing of aerodynamic load data from aerodynamics to structures and wing geometry deformations from structures to aerodynamics. This data transfer process was performed through two simple interface programs which demanded little or no modification to the aerodynamic and structural computer codes. In the aerodynamics to structures data transfer process, the pressure distribution computed from the aerodynamic analysis is integrated over a series of spanwise strips to obtain equivalent forces and moments, including hinge moments, for each strip. The resulting forces normal to the wing plane and the moments along the wing axis were then applied as concentrated external loads to the finite element grid points associated with each strip. Note that wing deformation due to frictional forces was believed to be minimal (compared with pressure forces), and therefore it was neglected for the Navier-Stokes analysis.

In the transfer of data from structures to aerodynamics, the displacement and rotation values computed at the finite element grid points were interpolated to a number of airfoil sections used to define the wing geometry. Each airfoil section was rigidly translated and rotated about the wing elastic axis according to the interpolated values. Control surface deflections due to the applied loads were approximated by rotating the appropriate portion of the airfoil section about the hinge point. For this study, only the displacement values normal to the wing plane and the rotation values about the wing axis were used. This is consistent with the forces and moments chosen for application to the finite element model.

The deformation of the aircraft wing throughout the aeroelastic iteration process can be seen in Figs. 7 and 8. The figures display various surface deflection and rotation values computed for the wing using both inviscid and viscous aerodynamic loading. In Fig. 7, the average deflection angles for the two leading-edge and two trailing-edge control surfaces along with the relative angle of attack of the wing tip (value does not include wing geometric twist) are plotted versus iteration number. The aeroelastic iteration history for the wing tip displacement is shown in Fig. 8. The values plotted for the zeroth iteration represent the initial rigid wing configuration while the values plotted for the first iteration represent the solution of the finite element model subject to the initial rigid wing aerodynamic loads. Convergence was assumed when the calculated airloads were consistent with the structural deflections. The convergence test was that the shape change between iterations (i.e., differences in the finite element deflection and rotation values) is less than a certain tolerance, taken to be approximately 3%.

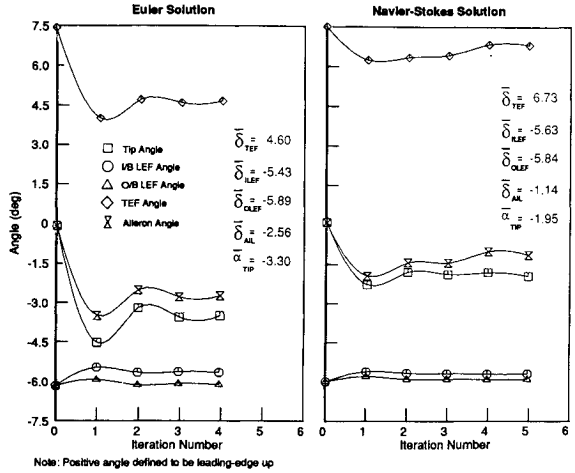

Fig. 7 Aeroelastic iteration history for wing tip and control surface angles.

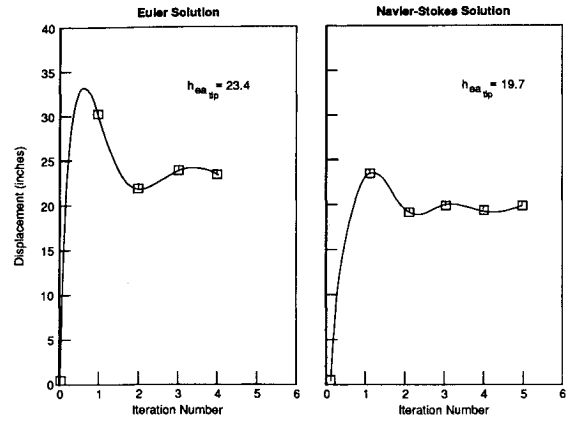

Fig. 8 Aeroelastic iteration history for the displacement of the elastic axis at the wing tip.

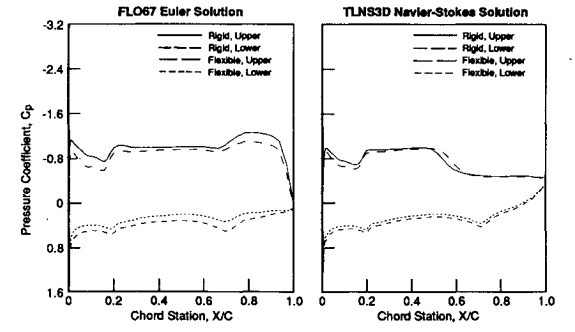

Fig. 9 Wing pressure distributions for the rigid and flexible geometries at 45% semispan location.

The inviscid aeroelastic results shown in Figs. 7 and 8 indicate a considerable amount of wing deformation. The wing tip, for example, has a final deflection (from the baseline geometry) of 23.4 in. (10% of the semispan) and an induced twist of 3.3 deg, leading-edge down. The loading also caused the control surfaces to deflect in the direction necessary to decrease the aerodynamic load. The control surface angles shown in the figure are defined relative to the wing incidence angle with the sign convention being positive leading-edge up/trailing-edge down.

The viscous aeroelastic results in Figs. 7 and 8 show wing deformations similar to the inviscid solution, but with smaller magnitudes. The principal reason for this is the large region of shock-induced separated flow on the aft portion of the wing. The separated flowfield produces a forward shift in the center of pressure which results in less aeroelastic twist. In addition, the trailing-edge loads are greatly reduced, which result in decreased trailing-edge flap and aileron aeroelastic deflections.

Figure 9 compares the chordwise pressures computed for the flexible and the rigid geometries at the 45% semispan location. Both the inviscid and the viscous aerodynamic solutions are included in the plot. As indicated previously, the effect of flexibility is to decrease the aerodynamic load over the wing and the control surfaces. This can be seen in the figure as a decrease in the difference between the lower and upper surface pressures. It can also be seen why an inviscid aerodynamic analysis would lead to greatly overpredicted loads at the trailing-edge in comparison to a viscous analysis.

Comparison Against Experiment

The Euler and Navier-Stokes solutions obtained above were used to compute the component loads, e.g., wing shear, torque, bending moment, and control surface hinge moments. The wing loads are given at both inboard and outboard locations. The component loads are computed by first defining a loads reference axis (LRA). Next, a reference or normal direction is chosen to be used with the LRA. All of this reference information is consistent with the loads measured during flight testing. Using the pressures from the CFD solution, the point loads at each node of the surface mesh were computed. Then the components of the CFD point loads in the direction of the reference direction are summed along the LRA to yield the CFD component loads. Any point loads beyond the end of the LRA are not used in the calculation of that component load. For example, all the point loads inboard of the wing fold reference point are not used to compute the outboard wing loads (Fig. 10). For the control surfaces, the hinge line of the surface is used as the LRA and only those CFD nodes on the control surface itself are used for calculation of the CFD hinge moments.

The flight test data represent a transonic design condition typical of fighter aircraft. The loads are measured only at discrete locations on the aircraft, therefore a detailed distribution of the flight loads is not available. In addition, the flight test loads are comprised of aerodynamic and inertial components. Since only the aerodynamic component is desired, the inertial portion has been subtracted out of the measured flight loads. All further remarks about the flight test loads will only refer to the aerodynamic component. Moreover, some of the flight loads can be more accurately measured than others. In general, wing bending moment is the most reliable flight load, while wing shear and wing torsion are less accurate. This is particularly true when the measured wing torsion is much smaller than the design limit torsion.

Table 1 displays the CFD and flight test loads. The data are arranged in order of increasing complexity starting with

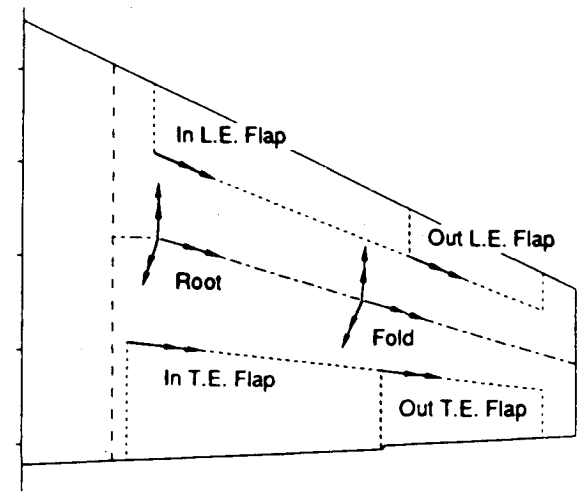

Fig. 10 Loads reference axis and control surface hinge lines for the fighter-like wing.

Table 1 Comparison between CFD and flight test loads for the fighter-like wing

Load	FLO67(W) Rigid, %	FLO67(W) Flex, %	FLO67(WB) Rigid, %	FLO67(WBT) Rigid, %	TLNS3D(W) Rigid, %	TLNS3D(W) Flex, %
Wing root						
BM	40.3	3.0	29.8	28.9	8.7	−1.2
TQ*	−8.3	−6.6	−8.2	−6.9	−3.3	−3.6
Wing fold						
SH	30.4	−7.0	22.1	19.6	−1.6	−9.5
BM	17.4	−19.0	6.9	6.8	−5.2	−19.1
TQ*	−10.8	−12.4	−11.5	−12.6	−7.6	−7.9
Hinge moments						
OLEF	−18.1	−59.0	−48.3	−45.1	−18.7	−40.1
ILEF	−29.5	−53.0	−46.9	−42.9	−28.2	−37.9
ITEF	278	119	169	154	59.0	54.6
AIL	117	75	128	123	45.6	16.5

$M_\infty = 0.90$, $\alpha = 10$ deg.
*Center of pressure error in % local chord.

the inviscid wing alone analysis and ending with flexible viscous results. For the wing shear, bending moment, and hinge moments, the values in Table 1 are the differences between the CFD and experimental loads as a percentage of the experimental loads. For wing torsion, the values are the difference in center-of-pressure locations measured in percent of the local chord. Since the torsion values are small, this is more descriptive of the quality of the torsion calculations. The CFD loads are considered acceptable when they are within 10% of the flight test loads.

Inviscid Results

To begin with, consider the inviscid rigid wing alone analysis. CFD greatly overestimates wing bending moment (BM) and wing shear (SH) at both the inboard and outboard stations. The best comparison is for outboard BM at 17.4%, which is still too large for adequate load prediction. In addition, the wing torque (TQ) shows a −8.3% difference at the inboard station and a −10.8% difference at the outboard station. While these results are much improved over the SH and BM, improvement is still needed at the outboard station. Finally, the CFD control surface hinge moments (HM) also show significant deviations from the flight data. The inboard and outboard leading-edge HM are underpredicted by 18.1% and 29.5%, respectively. Both the trailing-edge (flap and aileron) HM are overpredicted in excess of 100%. These results occur because the Euler solution cannot predict the shock-induced separation that occurs on the wing upper surface. As the flow expands around the wing leading edge, it becomes locally supersonic and remains that way until reaching a strong shock standing over the trailing-edge control surfaces. The relatively lower pressures in the supersonic flow on the wing upper surface, as compared to the subsonic lower surface pressures, yield component loads that are overpredicted, particularly the trailing-edge HM. This result was not obvious a priori, and was not understood until the viscous wing solutions were obtained.

Other factors also contributed to the differences between the computed and the flight loads. Among these are the interference effects on the wing by other parts of the aircraft geometry and the static aeroelastic effects due to the flexibility of the wing. The interference effects of the fuselage are shown in Table 1. In general, the presence of the fuselage improved the wing loads substantially. At the wing root, the BM error decreased from 40.3%, for the wing alone, to 29.8% for the wing-fuselage. At the wingfold, the wing SH error decreased by 8.3%, and the BM error decreased by 10.5%. The wing TQ error changed from −10.8%, for the wing alone, to −11.5%. Finally, both the inboard leading-edge flap (ILEF) and the outboard leading-edge (OLEF) HM errors increased by over 20%, whereas the inboard trailing-edge flap (ITEF) shows substantial reduction in the HM error. The aileron (AIL) HM errors showed increases over the wing alone results by 11%. The overall impact of the fuselage was to decrease the wing SH and BM, and slightly increase the leading-edge down TQ at the wing root while increasing it at the wing fold. The fuselage also decreased all of the HM. This follows since lower SH and BM loads will result in smaller HM as well. The fuselage itself has altered the circulation around the wing thus lowering the wing loads.

The interference effects of the fuselage and horizontal tail are also shown in Table 1. Compared to the wing alone loads, the wing SH and BM show improvement, but wing TQ improves only at the inboard station. The inboard BM goes from an error of 40.3% to 28.9%, and the outboard BM has an error of only 6.8%. The error of the inboard wing TQ becomes −6.9%, but at the outboard station the error increases to −12.6%. Compared to the wing-fuselage results, the horizontal tail decreases the wing BM and SH by less than 5% at both the root and fold. However the wing TQ shows improvement at the wing root, but not at the fold. Moreover, all of the hinge moments show improvement due to the interference effects of the horizontal tail, but only the ITEF shows a change greater than 5%. The inboard trailing-edge flap (ITEF) error reduces to 154%, down from 278% for the wing-alone and down from 169% for the wing-fuselage. This result is not surprising since the horizontal tail is in close proximity to the ITEF, but not the remaining control surfaces. In addition, the overall wing SH and BM change by less than 5% when the horizontal tail is added. Thus the interference effects of the tail are minor as compared to the fuselage, with the exception of the ITEF HM.

These mixed results indicate that while the interference effects of the fuselage and horizontal tail are important, they are not sufficient to yield reliable component loads. It is worth repeating that this analysis did not include the impact of the leading-edge extension (LEX).

The effect of flexibility on the inviscid wing loads is also shown in Table 1. To begin with, inboard wing BM shows a very good correlation with an error of only 3.0%. This compares with a 40% error for the rigid inviscid wing. In addition, the error in outboard wing SH goes from 30.4% to −7.0%. Unfortunately, the outboard wing BM has an error of −19.0%, which is not an improvement. Wing TQ shows improvement only at the inboard station. The error at the outboard station increases from −10.8% to −12.4%. The trailing edge HM shows major improvement, with the error of the ITEF going from 278% to 119% and the aileron (AIL) HM error reducing to 75% from 117%. On the other hand, the leading-edge HM shows significant degradation.

These results occur because the wing deforms by bending up and twisting the leading-edge down. In addition, all of the control surfaces reduce their deflections relative to the wing. These sorts of deformations reduce the magnitude of all the component loads by decreasing the expansion near the leading-edge, reducing the strength of the trailing-edge shock, and decreasing the pressures over the entire lower surface. The comparisons with flight data fail to improve primarily because

the inviscid pressures are not physically correct for reasons discussed above. Furthermore, the simplified structural model and the way the CFD surface grid smoothly blends the ITEF with the AIL also play a role in determining the CFD loads. These results demonstrate that, as with the interference effects, static aeroelasticity is important, but the effect is not large enough to yield reliable component loads unless other effects are considered.

Viscous Results

The final sets of loads shown in Table 1 are the rigid and flexible viscous loads. Starting with the rigid wing, the inboard BM error is 8.7% and the TQ error is only −3.3%. The errors at the outboard station for SH, BM, and TQ, are −1.6%, −5.2%, and −7.6%, respectively. The control surface HM also show dramatic improvement over all of the inviscid calculations, but the errors are still too high. For example, the outboard leading-edge flap (OLEF) error is −18.7% and the inboard leading-edge flap (ILEF) error is −28.2%. However, the ITEF and the AIL HM errors become 59.0% and 45.6%. These compare with 278% and 117% for the rigid inviscid wing case.

The overall improvement in the component loads described above arises primarily because the viscous solution predicts shock-induced separation over a large portion of the upper wing surface (Fig. 5). Near the leading-edge, the viscous flow behaves much like the inviscid flow. The flow expands around the leading-edge flaps and becomes supersonic. But near the 50% chord point, a shock forms and the flow separates behind it. Moving from inboard to outboard, the shock moves downstream and stands near the trailing-edge when the AIL is reached. This clearly shows that the deflected ITEF creates an adverse pressure gradient, whereas the undeflected AIL does not, and the flow remains attached. The relatively higher pressures on the wing upper surface in the separated case, as compared to the attached case, reduce all the component loads, particularly the trailing-edge HM. All of the wing loads are now within 10% of the flight data and could be used to predict design loads. The control surface HM still show sizable errors.

By including flexibility effects upon the viscous loads, in general no further improvement was obtained. Only one of the wing loads, the inboard BM, showed any improvement at all. Its error went from 8.7% to only −1.2%. The control surface HM also showed little or no improvement, except for the AIL HM. Its error dropped to 16.5%. The wing deflections are similar to the inviscid case, with the wing bending upward and leading-edge twisting down. But since the viscous loads are lower than the inviscid loads, the magnitude of the wing deflections are smaller. The effect of flexibility was to move the shock on the wing upper surface slightly aft and decrease the pressures over the wing lower surface. These effects together with the deficiencies mentioned in the inviscid results combine to degrade the comparisons between the CFD and flight test loads.

Summary and Conclusions

In summary, viscosity has the largest impact on the accuracy of design loads prediction for the fighter-like aircraft wing at this flight (high wing loading) condition. Interference and flexibility have only a secondary influence on the loads. These results show that design loads can be predicted well with a viscous rigid wing analysis. The analysis also implies that full aircraft Euler calculations may be of limited value for transonic loads prediction when very high load factors occur. Problems still remain in the prediction of control surface hinge moments. Future efforts should include more complete geometry, improved structural models, and a grid density study on the viscous wing to improve the HM predictions.

Acknowledgments

The authors are grateful to James D. Lang, Director of Flight Sciences, for both inspiring and supporting this effort. The authors also thank Thomas H. Burkhart, Raymond R. Cosner, Thomas A. Kinard, Dale A. Pitt, Timothy D. Smith, August Verhoff, and Ivo Zvolanek for their support and cooperation. Computer resources for this work were provided by the Numerical Aerodynamic Simulation (NAS) facility at NASA Ames Research Center.

References

[1]Huband, G. W., Rizzetta, D. P., and Shang, J. S., "The Numerical Simulation of the Navier-Stokes Equations for an F-16 Configuration," AIAA Paper 88-2507, June 1988.

[2]Olling, C. R., and Mani, K. K., "Navier-Stokes and Euler Computations of the Flow Field Around a Complete Aircraft," SAE Paper 881488, Oct. 1988.

[3]Whitlow, W., Jr., and Bennett, R. M., "Application of a Transonic Potential Flow Code to the Static Aeroelastic Analysis of Three-Dimensional Wings," AIAA Paper 82-0689, May 1982.

[4]Tatum, K. E., and Giles, G. L., "Integrating Nonlinear Aerodynamics and Structural Analysis for a Complete Fighter Configuration," *Journal of Aircraft,* Vol. 25, No. 12, 1988, pp. 1150–1156.

[5]Jameson, A., "A Vertex Based Multigrid Algorithm for Three-Dimensional Compressible Flow Calculations," *ASME Symposium on Numerical Methods for Compressible Flow,* Dec. 1986.

[6]LaBozzetta, W. F., Cole, P. E., Kreis, R. I., and Finfrock, G. P., "Configuration Data Management System," AFWAL-TR-87-3064, Vol. I and II, Dec. 1987.

[7]Thompson, J. F., "Program EAGLE Numerical Grid Generation System," AFATL-TR-87-15, Vol. II and III, Jan. 1987.

[8]Vatsa, V. N., "Accurate Solutions for Transonic Viscous Flow Over Finite Wings," AIAA Paper 86-1052, May 1986.

[9]Eriksson, L. E., "Transfinite Mesh Generation and Computer-Aided Analysis of Mesh Effects," Ph.D. Dissertation, Uppsala Univ., Sweden, March 1984.

[10]Johnson, D. A., and King, L. S.,"A Mathematically Simple Turbulence Model for Attached and Separated Turbulent Boundary Layers," *AIAA Journal,* Vol. 23, No. 11, 1985, pp. 1684–1692.

[11]Abid, R., Vatsa, V. N., Johnson, D. A., and Wedan, B. W., "Prediction of Separated Transonic Wing Flows with a Non-Equilibrium Algebraic Model," AIAA Paper 89-0558, Jan. 1989.

[12]MacNeal, R. H., "The NASTRAN Theoretical Manual," NASA SP-221(01), Dec. 1973.